 doi:10.20944/preprints202108.0504.v1

Communication

A Miniature Permanent Magnet Assembly with Localized and Uniform Field with an Application to Optical Pumping of Helium

Garnet Cameron [1,*], Jonathan Cuevas [1], Jeffrey Pound Jr. [1] and David Shiner [1]

[1] Physics Department, College of Science, University of North Texas, 210 Avenue A, Denton, TX 76203, USA; garnetCameron@my.unt.edu
* Correspondence: garnetCameron@my.unt.edu

Featured Application: atomic laser spectroscopy

Abstract: Atomic state preparation can benefit from a compact and uniform magnetic field source. Simulations and experimental measurements have been used to design, build, and test such a source as shown by optical pumping of atomic Helium. This source is a 9.5 mm (3/8") OD x 6.7 mm (1/4") ID x 9.5 mm (3/8") long, NdFeB-N42 assembly of 1.6 mm (1/16") thick customized annular magnets. It has octopole decay with a residual dipole far field from imperfect dipole cancelations. It has greater than 50% clear aperture with uniform and collimated magnetic field consistent with the prediction of several models. Octopole roll-off localizes the field minimizing the need for shielding in applications. The device is applied to a high precision ^{3,4}He laser spectroscopy experiment using σ^+ or σ^- optical pumping currently resulting in a measured 99.3% preparation efficiency and in accordance with a rate-equation model.

Keywords: optical pumping; annular permanent magnet; miniature magnet; laser orbital angular momentum; collimated magnetic field; fringe magnetic field

1. Introduction

In atomic state preparation, often a circular polarized, broadband laser uses orbital angular momentum transfer to migrate multiple transitions to a desired bounding spin state [1]. A magnetic field can be used to define and maintain the quantization z-axis. The physical dimensions of the magnetic field and its source are a significant concern. Ultra-High Vacuum (UHV) experimental system components often vie for cavity space and can force trade-offs in overall experimental optimizations. An intended application of this magnet assembly is an existing atomic laser spectroscopy experiment that has evolved through at least three versions since 1995 [2-4] starting from ^{4}He with 51 ppb precision results [2]. It is now capable of simultaneous measurements of ^{3}He and ^{4}He isotopes at 20 ppb [4].

Preprints (www.preprints.org) | NOT PEER-REVIEWED | Posted: 26 August 2021 doi:10.20944/preprints202108.0504.v1

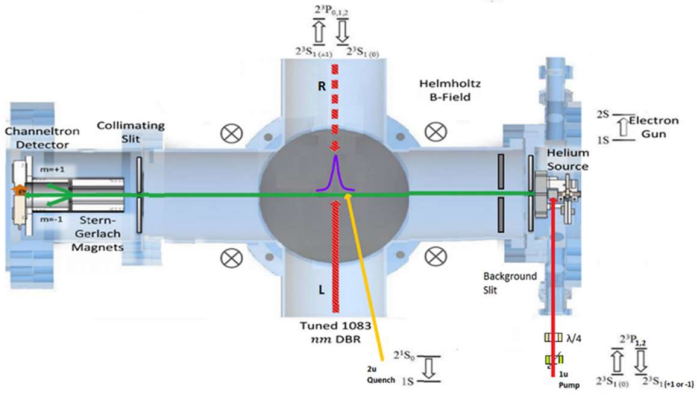

Figure 1. Atomic Beam Apparatus: Helium Source is the area of interest.

The Atomic Beam apparatus is shown in Figure 1. Metastable Helium atoms (He*) are prepared into $1s^1 2s^1$ electronic configuration via ~20 eV electron bombardment in the Helium Source at the right end of the green atomic beam. An approximately 50-50 mixture of singlet and triplet He* atoms is created. The triplet, 2S, $m_j = 0$ ($2^3S_{1,m_j=0}$) Zeeman level is prepared as the experiment signal channel by optically pumping to zero population. Preparing the atomic beam with a circular polarized laser instead of the previous linearly polarized laser doubles our signal size by sweeping the atoms into either +1 or -1 magnetic state versus splitting the population between the two. Retarders are used to transform an incoming linear polarized 1 μm laser to σ^+ or σ^- polarization.

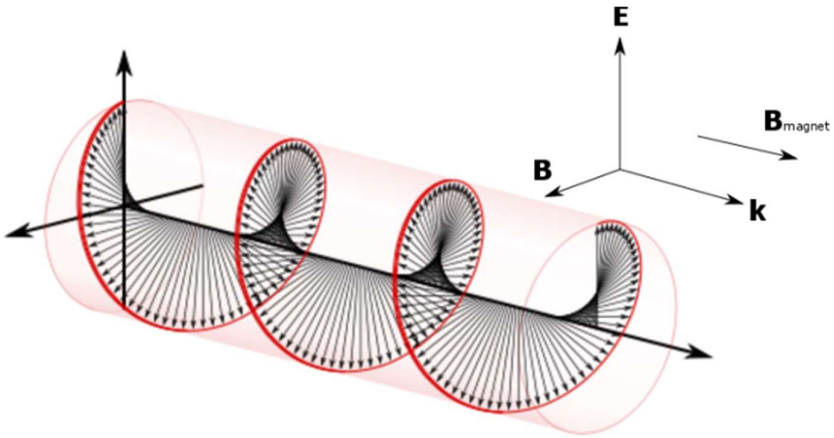

Figure 2. Atomic Beam Preparation Laser Polarization, **k**, and $\mathbf{B}_{\text{magnet}}$ arrangement (Right or σ^+ shown).

According to quantum mechanical selection rules, increasing or decreasing angular momentum m_s by laser stimulation demands [X][Y] transitions or $\Delta m_j = \pm 1$ [4]. The laser E-field (polarization) should be perpendicular to the quantization axis (z) defined by an imposed B-field ($\mathbf{B}_{\text{magnet}}$). As suggested by Kastler [1], laser propagation (**k**) parallel to $\mathbf{B}_{\text{magnet}}$ guarantees this requirement for a circularly polarized laser, as shown in Figure 2. A permanent magnet is a passive and compact magnetic field source versus high current and turns-dense solenoids with associated heating issues. Since the 1980's, NdFeB permanent magnets have offered the highest available range of maximum energy products [5]. N42 grade is an economical choice for prototyping, but carries a low Currie Point of 80 °C. We focus on design, construction, and application of the preparation laser magnet.

2. Magnet Requirements and Dimensions

Preprints (www.preprints.org) | NOT PEER-REVIEWED | Posted: 26 August 2021 doi:10.20944/preprints202108.0504.v1

Our legacy atomic experiment 10^4 counts in each counting interval translates to a Poisson noise threshold of 1/100 by $\varepsilon = \sigma/\sqrt{N}$, where ε is error, σ is standard deviation, and N is quantity of events [6]. This threshold is expected to continue into projected higher signal levels coupled with reduced count interval time length. Electromagnetic energy is proportional to B^2. Therefore, at least 1/10 directional sensitivity of perpendicular polarization to the magnetic field is sought. Gaussmeter measurements around the neighboring electron gun magnets that use a return flux yoke revealed a 5 G perpendicular surrounding field suggesting a 50 G minimum preparation magnetic field strength.

Any fringing field in the spectroscopic laser interaction region needs to be minimized. Helium energy levels change at ~1.4 MHz/G, so sub kHz precision in helium spectroscopy makes field gradients of ~ 1 mG/mm desirable. The atomic beam pump laser is approximately 3.5" from the interaction region as seen in Figure 1. The far field is thus defined as greater than 3" removed from the preparation magnet center. Shielding would impact other needed magnetic fields in the apparatus.

Avoidance of experiment apparatus redesign prefers the magnet assembly to fit in the existing space for linear polarized atomic beam pumping. The critical dimensions are 3/8" along the atomic beam line (outer diameter of annular magnet) while providing enough atomic beam pumping transit distance to allow a minimum 90% and preferred 99% or better pumping to m_s = +1 or -1 (internal diameter). Figure 3, upper left corner shows a cross-sectional layout.

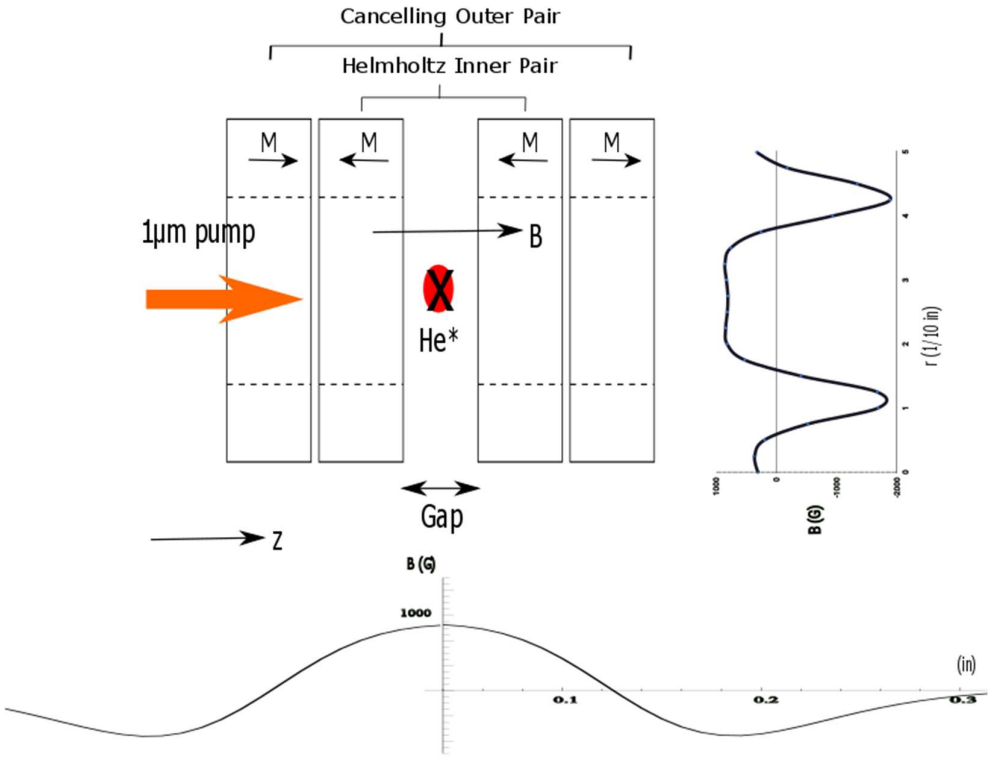

Figure 3. Created Magnet Assembly: bottom, axial (z) B_z field; right: mid-plane transverse (x or ρ) B_z field.

Faraday isolators like Gauthier's design [7] offer some inspiration towards the fringe field requirement. As shown in Figure 3, stacked pairs of magnets with opposed magnetization sum to a zero far field. The central field is collimated in Helmholtz fashion as the parallel magnetized pair of magnets straddling the Gap dominates there.

It is important to note that coincident points on axial (z-axis) and transverse (x-axis or ρ due to cylindrical symmetry) B-field profiles within the Gap must have the same

Preprints (www.preprints.org) | NOT PEER-REVIEWED | Posted: 26 August 2021 doi:10.20944/preprints202108.0504.v1

value i.e. the physical center point. Axial (z) and transverse (x or ρ) B_z-field plots are shown in the bottom and right of Figure 3, respectively. Areas beyond 3" from the Gap center comprise the far field while the Gap is labelled.

3. Design and Construction

Magnetic fields are solved in two ways. A quick axial/longitudinal (z-axis) solution can be determined by Biöt Savart current coil model summation. Alternatively, Finite Element Analysis (FEA) using Maxwell's Equations [8] provides a more complete solution profiling longitudinal or z-axis, and transverse or x-axis B-fields.

$$\vec{H} \equiv -\vec{\nabla}\Phi$$

$$\vec{\nabla} \cdot \vec{B} = 0$$

$$\vec{B} = \mu\left(\vec{H} + \vec{M}\right)$$

H is magnetic field strength, Φ is scalar magnetic potential, B is magnetic field intensity, and M is magnetization. Outside the magnetic material, M = 0:

$$\vec{\nabla} \cdot \vec{B} = \mu_0\left(\vec{\nabla} \cdot \vec{H} + \vec{\nabla} \cdot \vec{M}\right) \Rightarrow 0 = \mu_0\left(\vec{\nabla} \cdot \left(-\vec{\nabla}\Phi\right) + 0\right) \Rightarrow 0 = \nabla^2\Phi$$

Inside magnetic material bulk of constant magnetization, $\vec{M}$= constant. Magnetization may change on the magnet edges due to mutual coercion with other magnets. Closeness of simulated and measured values described later indicates that this effect is a small contribution.

$$\vec{\nabla} \cdot \vec{B} = \mu_0\left(\vec{\nabla} \cdot \vec{H} + \vec{\nabla} \cdot \vec{M}\right) \Rightarrow 0 = \mu_0\left(\vec{\nabla} \cdot \left(-\vec{\nabla}\Phi\right) + 0\right) \Rightarrow 0 = \nabla^2\Phi$$

For FEA modelling, $\vec{B}$ parallel to the surface or *Dirichlet* boundary condition (BC) is applied to the far bounding surfaces while $\vec{B}$ perpendicular to the surface or *Neuman* BC is employed at symmetry faces involving or very close to the magnet(s) e.g. the floor in Figure 4. The model space is reduced by exploiting symmetry planes to minimize simulation overhead. The whole solution is generated by duplicating the minimized volume.

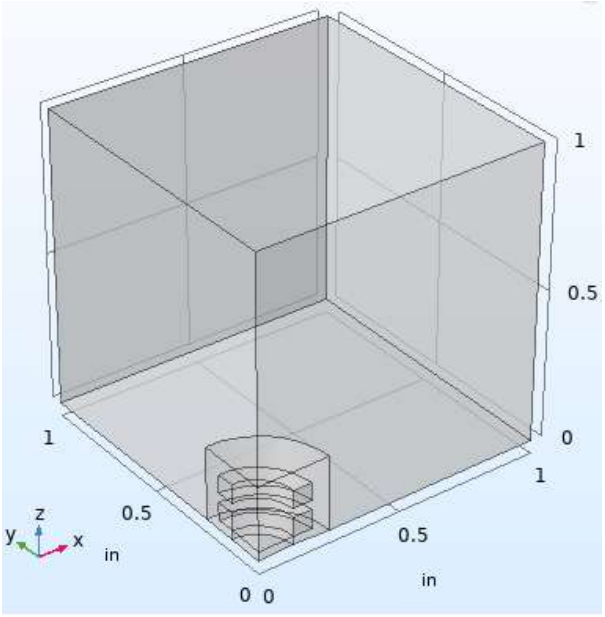

Figure 4. Reduced FEA Simulation Volume.

Preprints (www.preprints.org) | NOT PEER-REVIEWED | Posted: 26 August 2021 doi:10.20944/preprints202108.0504.v1

Exploration FEA simulations shown in Figure 5, examine different configurations of similar annular magnets. Clearly, a parallel magnetized pair stabilizes the central field. Addition of a repelling pair (one on each end) reduces the far field decay distance.

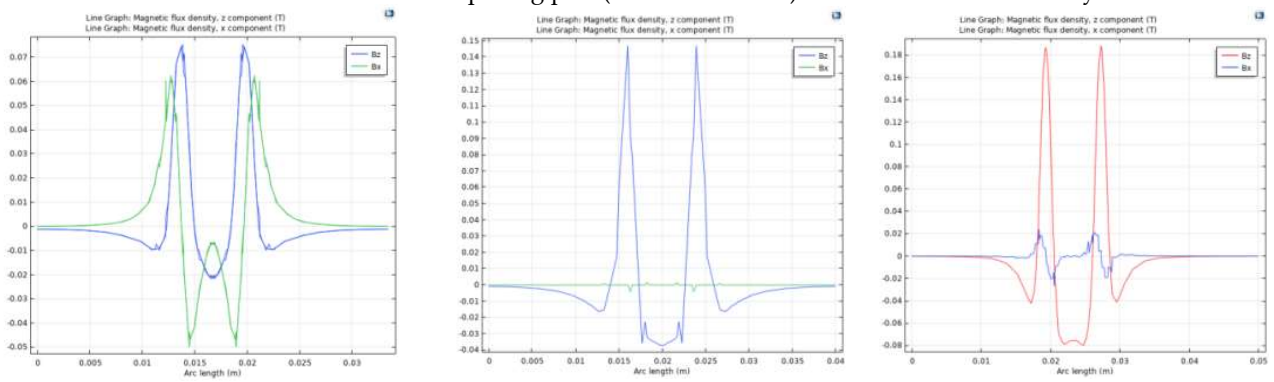

(a) (b) (c)

Figure 5 Simulated Transverse B_z and B_x for: **(a)** Single; **(b)** Pair; and **(c)** AR stack. Note: COMSOL [8] generated arbitrary positive and negative B sense is inverted compared the rest of our analysis.

3.1. B-field Collimation

Magnet dimensions were selected by Biöt Savart current coil approximation simulations [9] exploring axial B-field strength along the magnet assembly z-axis as the Gap size is varied as seen in Figure 7 (a). Code for all models is provided at https://github.com/garnetc/CircularLaserMagnet. Each magnet is modeled as a pair of inner and outer coaxial, z-centered, and counter rotating current loops. Multiple pairs of loops were simulated and found unnecessary – only a central pair was sufficient. Summation of infinitesimal magnetization current loops across the magnet bulk yields the current loops model [9].

From the Biöt Savart law:

$$d\vec{B} = kI\frac{\left(d\vec{l}\times\vec{r}\right)}{\left|\vec{r}\right|^3}$$

where, k is the magnetic constant, I is current, and r is the point of interest position. The well-known analytical solution of axial field for a circular coil is [10]:

$$B_{z,axial} = \frac{\mu_0 I}{2}\frac{r^2}{\left(z^2+r^2\right)^{3/2}}$$

Therefore, the assembly axial field $B_z(z)$ is a summation over all the coils/magnets:

$$B_z(z) = \frac{\mu_0 I}{2}\left\{\sum_{\substack{i=2,3\\ j=1,2}}\frac{(-1)^j r_j^2}{\left[\left(z-z_i\right)^2+r_j^2\right]^{3/2}} - \sum_{\substack{i=1,4\\ j=in,out}}\frac{(-1)^j r_j^2}{\left[\left(z-z_i\right)^2+r_j^2\right]^{3/2}}\right\}$$

The magnets are numbered left to right, 1 to 4 and are indexed as i. The inner and outer coils are represented by j and are numbered 2 and 1, respectively.

Antiparallel magnetization directions sum depending on Gap size. Axial (z-axis) field strength is also influenced by the ratio of inner radius (R_i), outer radius (R_o), and thickness of each magnet. In Figure 7 (c), solenoid simulation identifies the optimum thickness and R_i/R_o values. However, thickness and outer diameter (OD) selection were constrained by commercially available options: 1/8″ or 1/16″ and OD ($2R_o$) desired to 3/8″ (mentioned earlier), respectively. Conceptually, smaller thickness would be preferable

Preprints (www.preprints.org) | NOT PEER-REVIEWED | Posted: 26 August 2021 doi:10.20944/preprints202108.0504.v1

when the annular magnet is modelled as inner and outer solenoids. Thicker magnets relative to outer diameter tend to the infinite coil solution where the axial fields sum vanishes - axial fields of the inner and outer coils are equal and opposite. Jackson's [9] (p. 225) solenoid-faces-subtending-angles solution shows this behavior:

$$B_{z,axis}(\theta_1,\theta_2) = \frac{\mu_0 NI}{2}(\cos\theta_1 + \cos\theta_2)$$

$$B_{z,axis}(\theta_1,\theta_2) \lim_{\theta_1=\theta_2\to 0} \mu_0 NI$$

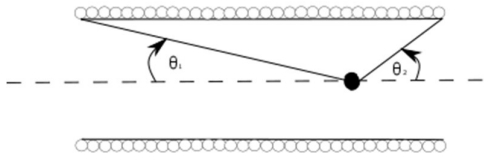

Figure 6. Thick-Magnet Axial Field Behavior (N = coil turns per length, I = current).

In other words, the outer loop negative impact on the sum axial (B_z) field is reduced by largest possible OD. Experiment apparatus 3/8" available space therefore sets the OD.

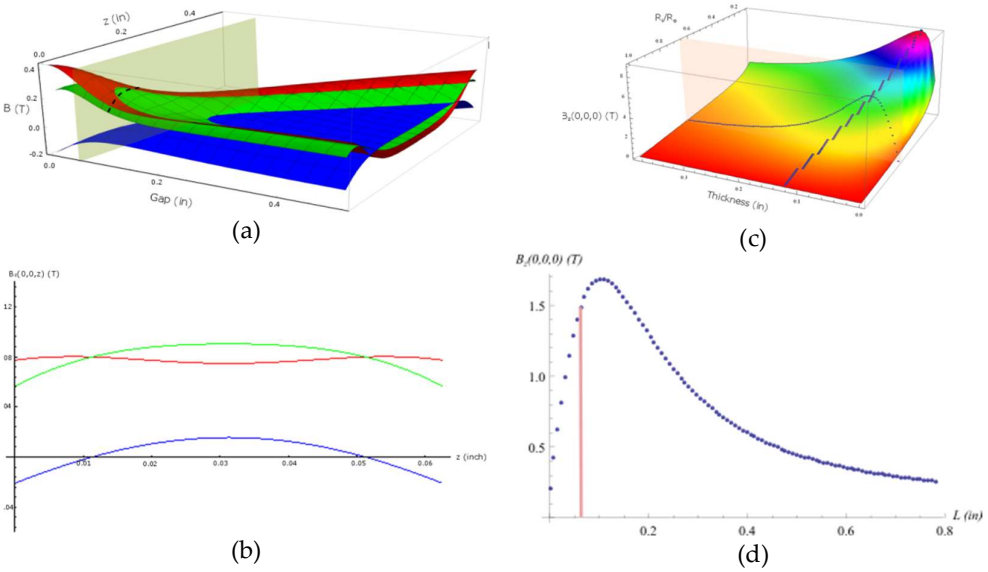

Figure 7. Simple Biöt Savart Axial (z-axis) Simulation Plots:

(a) B_z(z, Gap) – Attracting Pair (Red), Repelling Pair (Blue), Sum (Green), system position slice and sum curve (shaded plane and dotted line);
(b) B_z(z, Gap = 0.125"), 0.125" Gap size due to coils modeled at the center point of 1/16" thick magnet i.e. actual Gap (1/16") + 2 * coil offset (1/32") – Attracting Pair (Red), Repelling Pair (Blue), Sum (Green);
(c) Single Magnet Face Center B_z(Ri/Ro, thickness) – colored Ri/Ro iso-bands highlights ratio behavior, maximum values (Black dots), system slice and curve (shaded plane and green broken curve);
(d) Single Magnet Face Center B_z(R_i/R_o = 0.67, thickness) – system position (red line)

3/8" OD constraint and commercial unavailability of 3/8" x 1/4" x 1/16" forced customization of 3/8" x 1/8" x 1/16" via Dremel-lathe working to widen the 1/8" inner diameter (ID) to 1/4" to allow sufficient atom transit time as discussed shortly.. Commercial annular magnets are sintered powders encased in a thin metallic jacket; in this case Ni-Cu-Ni. Usual cutting tools result in fracturing and disintegration. Grinding is the only viable option. The four customized annulars were evaluated for geometric individuality. 0.7% variance in thickness was the most differing characteristic noted. Figure 9(a) shows the typical measured transverse (x-axis) B_z profile for a single annular. Center face "surface" field is ~400 G and center ring surface field is ~1600 G. K&J Magnetics (manufac-

 doi:10.20944/preprints202108.0504.v1

turer) [11] depicts the original 1/8″ ID annular B_{ring} to be ~1600 G as presented in Figure 8. However, more precise face center measures exhibited ~10% departures from theoretical/simulated values by K&J Magnetics for the 1/4″ ID e.g 441 G versus 487 G. Our precise measurements took account of a Lakeshore 450 Guassmeter 30 mils standoff of the active area from the contacted surface. Some hypotheses to explain the reduced field include localized ID grain boundary damage due to grinding or overall magnetization reduction during grinding despite cooling precautions. As a result, all in-house simulation work is referenced to the Gap center measured B-field.

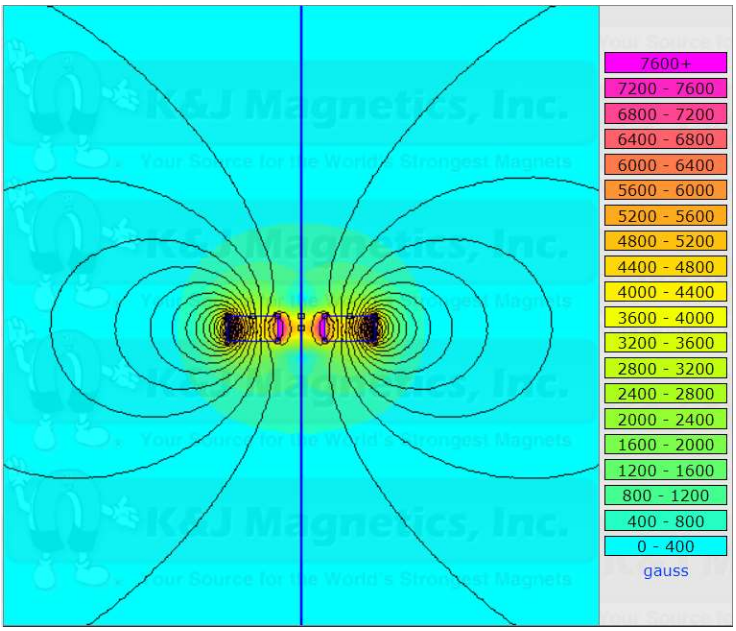

Figure 8. Magnetic Field Visualization of 3/8″ x 1/8″ x 1/16″ Annular [11].

Colloidal graphite was used to stabilize the exposed surfaces and minimize stray pump laser reflections. An Ultra-High Vacuum (UHV) chamber compatible mount was manufactured retaining the 1/16″ Gap, illustrated in Figure 9. 80 mil and 180 mil vertical gap versions allowed vacuum experiment and bench probing, respectively. Profile results are shown in Figure 10 revealing a 0.1″ to 0.15″ collimated B-field diameter

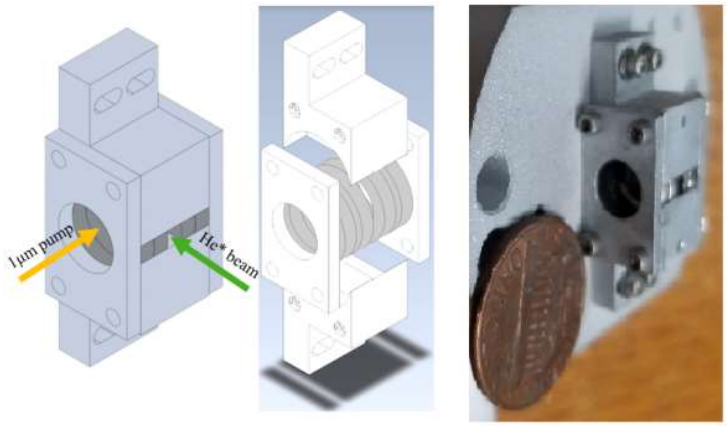

Figure 9. UHV Atomic Beam Pump Magnet Mount.

Preprints (www.preprints.org) | NOT PEER-REVIEWED | Posted: 26 August 2021 doi:10.20944/preprints202108.0504.v1

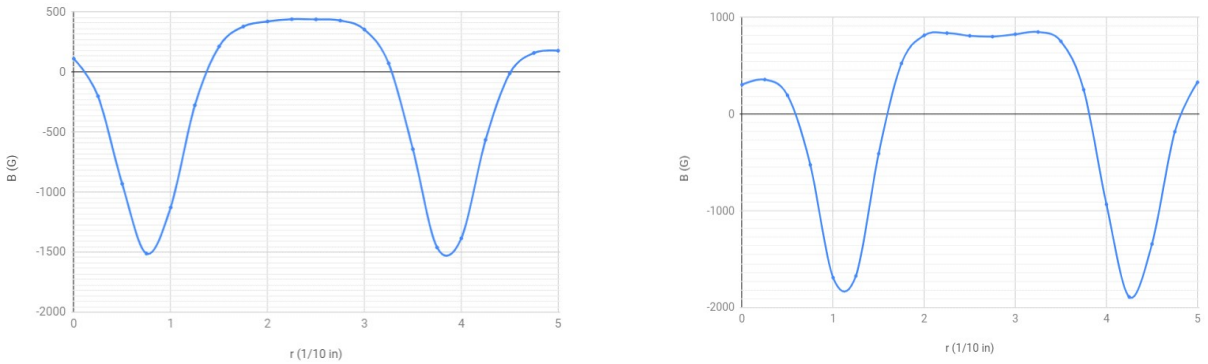

(a) (b)

Figure 10. Atomic Beam Pump Laser, 3/8" x 1/4" x 1/16" Magnet Transverse B-field Profiles: (a) Single; (b) Assembly.

1/4" ID was selected based on minimum atom travel distance, d, dictated by the number of atomic beam cycles, n, to allow 1/100 depletion of the 2^3S_1:m_j=0 level. The pump/applied laser will be broad bandwidth covering all possible transitions ($\Delta m_j = 0$). A simplistic estimate of the signal channel population, N, is achieved from the single excitation remaining ratio (portion of atoms still in 2^3S_1:m_j=0 state), r, excitation life time, τ, number of excitations/cycles, n, and atom velocity, v_{rms}.

$$N = N_0 r^n \Rightarrow n = \log\left(\frac{N}{N_0}\right) \Big/ \log r \tag{1}$$

$$d = v_{rms}\left(n\tau\right) = v_{rms}\tau \log\left(\frac{N}{N_0}\right) \Big/ \log r \tag{2}$$

r can be assessed by examination of excitation and relaxations paths assuming similar transition probabilities and branching ratios. A simplified three-level transition scheme [12] is shown in Figure 11. Atoms are coherently excited from Level 0 (representing our 2^3S_1:m_j=0) to Level 2 (all excited states). Relaxation de-coherently branches equally between Level 0 and Level 1 (destination spin state). Therefore, r is 0.5. τ is treated as twice the natural lifetime due to Level 0-Level 2 cycling.

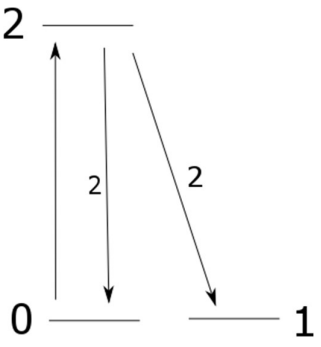

Preprints (www.preprints.org) | NOT PEER-REVIEWED | Posted: 26 August 2021 doi:10.20944/preprints202108.0504.v1

Figure 11. Simplified Three-level Schematic.

$$v_{rms} \cong 1500\, m/s$$
$$\tau = 2 \times 100 = 200\, ns$$
$$N / N_0 = 0.01$$
$$r = 0.5$$
$$d = 1500 \times 2E-7 \times \log(0.01)/\log(0.5) = 1.99\, mm = 0.078\, in$$

This minimum of 0.08 inch He* beam travel distance requirement is an infinite power result for an average velocity. In addition, alignment tolerances and edge inhomogeneity may also degrade performance, so we take a 0.15 inch diameter of collimated B-field as a more realistic minimum estimate. Zero B-field measured along the transverse (x) direction implies collimated B-field in the axial (z) direction.

3.1.1. Atomic Beam B-Field Collimation Precision

It is important to note that field profile shape differences between Biö Savart simulation (Figure 7 (b)) and the experimental (Figure 12 (b)) stems from axial versus transverse independent variable - z versus x or y (z-axis rotation symmetry), respectively.

The rectangular cross section atomic beam flows in the x-direction. It is 2 mils (50 μm) wide in the magnet longitudinal direction (z) and 80 mils (2 mm) tall (y). Longitudinal (z) B-field variation has small effect across the 2 mil range. But, transverse (x) B-field variation has significant impact across the possible 80 mils expanse and pump laser beam diameter. The empirically measured dip shown in Figure 10 (b) is 50 G compared to 800 G at the shoulders (~6%) over the 150 mil collimated B-field widow may be of concern and is considered in more detail below (Section 5 and Figure 15).

3.2 3-D Simulations

3-D simulations model more completely the physical situation (despite z-axis rotational symmetry) therefore providing more accurate values, and both axial (z-axis) and transverse (x-axis) profiles. EMS [13] - a Solid Works add-in by EM Works, and COMSOL (along with the Biö Savart summations and experimental readings) were used to produce the longitudinal (z-axis) and transverse plots (x-axis) shown in Figure 12**.**

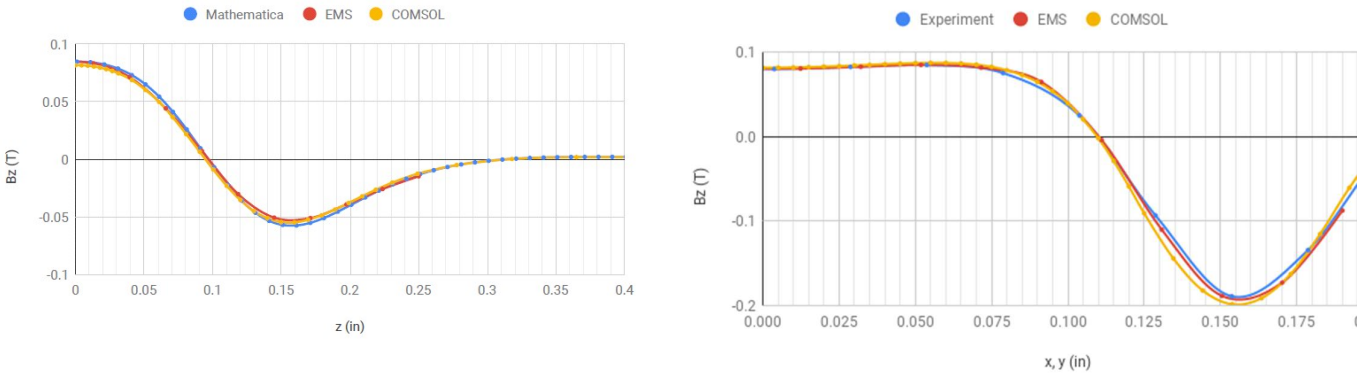

(a) (b)

Figure 12. B_z Combined Plots – Origin at symmetry axis: (a) Longitudinal (z-axis). Google Sheets resolution does not display clearly ~60 G dip at the origin; (b) Transverse (x-axis).

The simple axial/longitudinal Biö Savart Mathematica-based discrete current loop model compares favorably with EMS and COMSOL simulations. Similarly, EMS and

 doi:10.20944/preprints202108.0504.v1

COMSOL fit well with transverse experimental measurements in most of the Gap region. However, some separation is noted near the ID edge (0.125") and across the annular rims that end at 0.1875". EMS tracks closer. EMS operates on a hysteresis curve model while COMSOL was pinned to constant magnetization in the magnet bulk. One may hypothesize some small mutual coercive effects are present in the annular rim. In addition, some aperture effect occurred for the Lakeshore 40 mil diameter active area probe. The 50 s central dip is apparent in the transverse plot (x-axis).

4. Far Field Performance

Minimizing the stray field, ideally below our measurement uncertainty of 0.01 G, at the 3.5" distant interaction region is another important requirement for this magnet. Helium energy levels change at ~1.4 MHz/G. Measuring frequencies to kHz precision needs mG B-field consistency. Significant fringe field differences are noted for small spacing changes in Helmholtz Inner Pair and Cancelling Outer Pair as shown in Figure 13. Greater attention is paid to the z = 0 far field behavior because the subsequent precision spectroscopy interaction region is largely in the z = 0 plane of the magnet assembly (see Fig. 1).

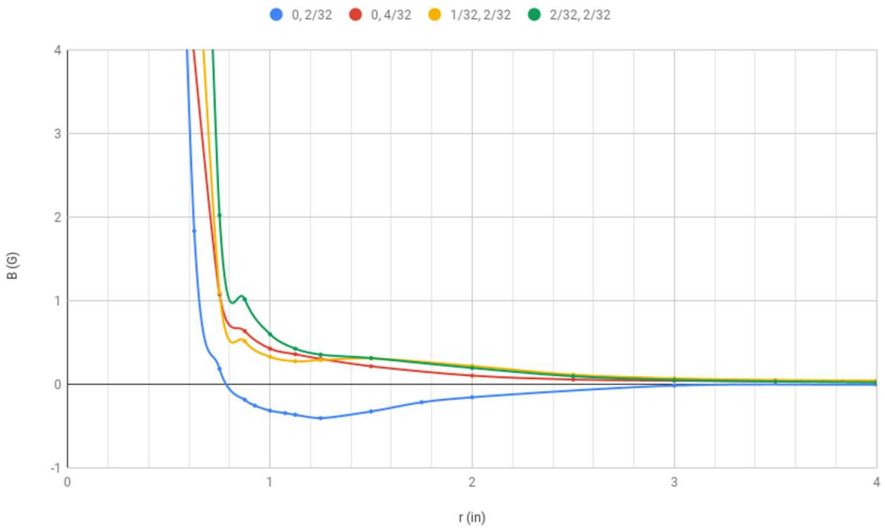

Figure 13 Transverse (ρ) Far Field B_z Measurements for "Inner-Outer Pair Separation, Gap" Variations

(at 3": 0, 2/32 = -0.020 G; 0, 4/32 = 0.038 G; 1/32, 2/32 = 0.066 G; 2/32, 2/32 = 0.047 G)

The 1/16" inner pair gap with no inner to outer spacing (0, 2/32) configuration exhibits anomalous behavior with a negative B-field inflection point. It nevertheless meets the 3" far field requirement with better performance than all other configurations presented. Transverse (x) asymptotic behavior was explored using the (0, 4/32) configuration to allow more fruitful model comparison as shown in Figure 14. Bz-field roll-off is compared with $1/r^5$ decay (blue broken line) and the COMSOL model prediction.. At sufficiently large distances (close to the noise level of our measurements), it appears that the imbalance in the individual cancelling dipoles of the configurations leads to a residual dipole component in the decay .

Preprints (www.preprints.org) | NOT PEER-REVIEWED | Posted: 26 August 2021 doi:10.20944/preprints202108.0504.v1

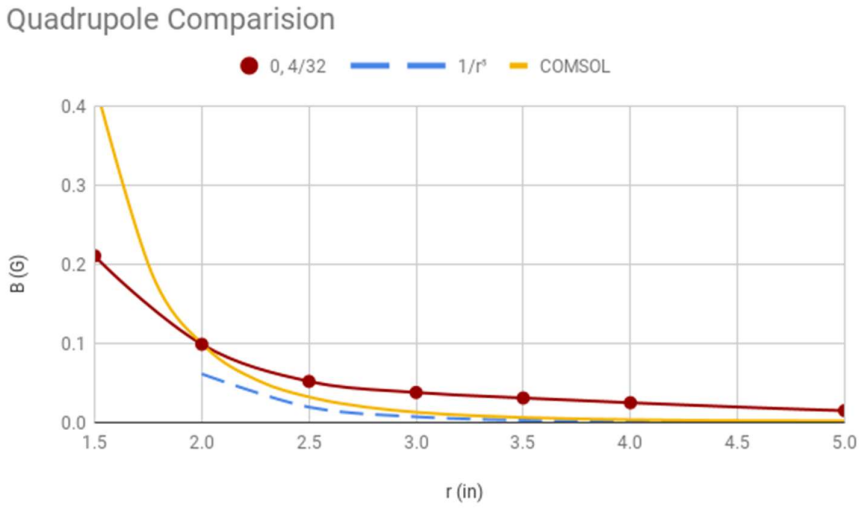

Figure 14. Far Field Asymptotic Behavior and $1/r^5$ (blue broken line).

5. Collimation Performance

Sensitivity to longitudinal (z-axis) atomic beam position was investigated via simulations. Findings are shown in Figure 15. Atomic beam z-position at the preparation point can be forgiving theoretically to almost 30 mils from center based on our 1/10 or 80 G B_x-threshold requirement as seen in (b). Better than 10 mils of positioning precision is typical for the apparatus. Of important note however, is that B_x at 1 mil z-offset (purple curve) shows significant increase reaching ~50 G at x = 125 mils (ID edge). Since atomic beam z-positioning is between 1 to 10 mils z-offset in practice, exposure to B_x greater than 80 G is possible beyond x = 80 mils. Polarization purity would be adversely effected by this field on the atomic beam exit side of the preparation area.

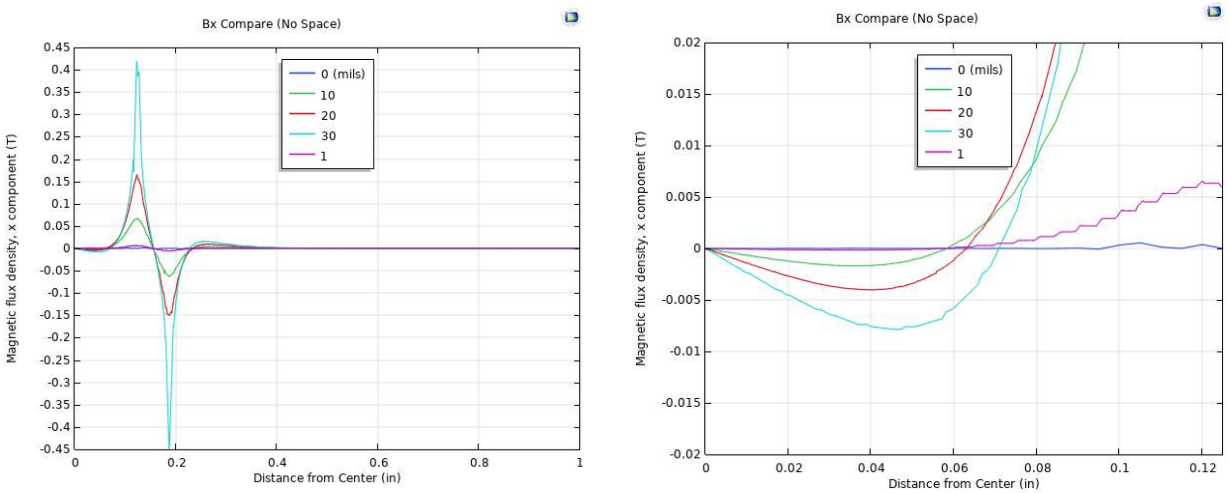

(a) (b)

Figure 15. B_x(x or y) at Varying Longitudinal Offset (z-axis, in mils): (a) Wide; (b) Span Inner Pair Gap (No inner to outer pair spacing).

The figure of merit for He* preparation is the survial ratio – portion of $2^3S_{1,\,m_j=0}$ remaining. from the He* mixture produced in the electron-bombardment source. The

Preprints (www.preprints.org) | NOT PEER-REVIEWED | Posted: 26 August 2021 doi:10.20944/preprints202108.0504.v1

relevant radiative excitation and relaxation paths for σ^+ ($\Delta m_s = 1$) are depicted in Figure 16. σ^+ and σ^- excitations are symmetric about $m_s = 0$.

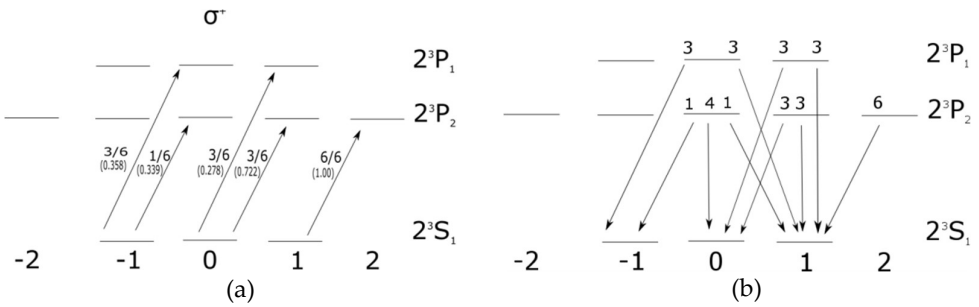

Figure 16 σ^+ ^{4}He Excitation and Relaxation Electric Dipole Matrix Elements (0 G): (a) Excitation, values in parentheses for 810 G ; (b) Relaxation [14]

The following rate equation quantifies the population behavior at level i, N_i, based on normalized electric dipole matrix elements D_{ik} for transitions between levels i and k as dictated by the laser polarization, σ, e.g. σ^+ polarization [15] (p.518). Equal laser power is assumed across all energy levels.

$$\frac{dN_i}{dt} = \sum_{k=\{\sigma\}} D_{ik}N_k - D_{ik}N_i$$

Figure 17 shows survival ratio with increasing laser power. Two features are apparent in (a): the model predicts sharper population decline than observed and close to complete clearing is achieved experimentally. The best ratio is ~99.3%. B_z fringe effect presented in Figure 15 (b) is theorized as cause for higher survival with intermediate laser power. Atomic beam exit side aperturing of the laser is being investigated.

Exponential decline in signal channel population with laser power is expected by the higher population of photons impinging the atomic beam and modulated by the atom-photon cross section [16] as assumed in Equation (2). Stimulation is occurring for many transitions between magnetic field dependent energy levels that are reachable by the ~2 GHz bandwidth and ~2mm waist laser as shown in Figure 11. Reaching 99.3% clearing is a validation of B-field 1/10 collimation nonetheless. Otherwise, significant parallel polarization ($\Delta m_s = 0$) transitions would wash-out clearing by returning atoms to the signal channel even at low power. Transit time constraint is known to be power independent from previous work [4].

Figure 17 (b) adds detail to the high power or infinite power asymptote survival ratio. A pure $\Delta m_j = +1$ model (Model) predicts 0.01% survival while we measure 0.7%. A modeled 0.07 rad misalignment of $\vec{k}$ and $\vec{B}$ (Model 0.07) matches the measured survival asymptote casting further interest on the Gap fringe field mentioned earlier. Modelling results are the same for 0 G and 810 G within experimental uncertainty. In addition, low to intermediate power survival ratio turbulence hinted in (a) is now clearly visible in (b). The Yb-doped fiber preparation laser is known to hop between 3 MHz separated modes (50 m cavity) therefore stimulating the 1.6 MHz FWHM transitions in fluctuating fashion.

Preprints (www.preprints.org) | NOT PEER-REVIEWED | Posted: 26 August 2021 doi:10.20944/preprints202108.0504.v1

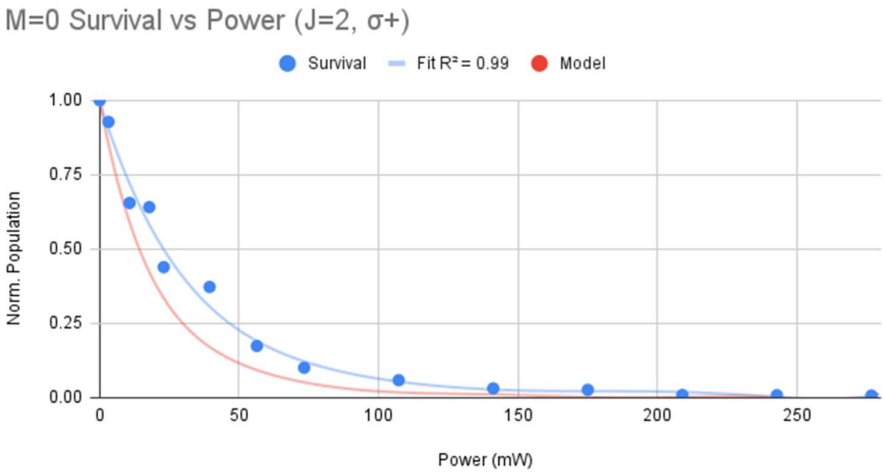

(a)

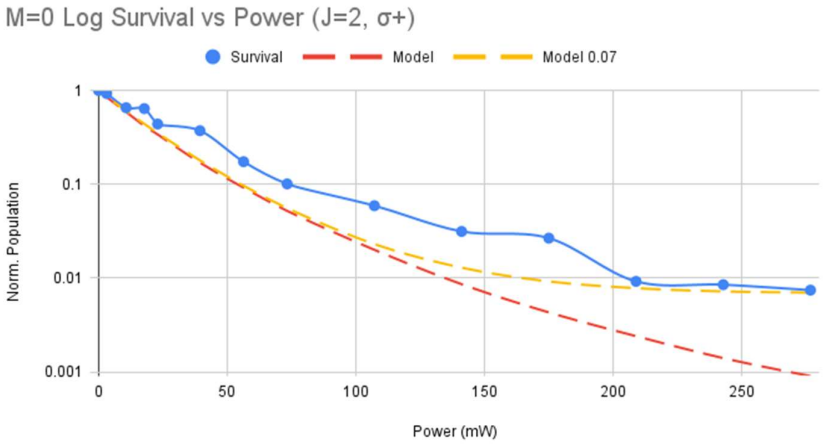

(b)

Figure 17. Preparation Laser Survival Ratio (1μm, σ+/left) vs Power: (a) Linear Plot and Base Model; (b) Log Plot and 0.07 rad Misalignment Model.

Experimentally, zero/near-zero B-field transit between source and detector causes helium beam depolarization as Zeeman energy level separations disappear/narrow. Interaction region Helmholtz coils are used as a precaution against such B-field zeros..

6. Conclusions and Further Work

This miniature magnet has been shown to present an 800 G, well collimated axial B-field (z-axis) to better than 1/10 as verified by simulation, table top measurements, and atomic experiment. The fringe field falls as an octopole ($1/r^5$), reaching a small residual dipole far field (arising from imperfect dipole cancelations) in less than 3" (7.6 cm), as determined by both simulation and experiment. Any space constrained application needing a non-shielded, localized, and well collimated magnetic field source can benefft from this device or similar design.

Some improvements possible from this effort are:

1. ***Further preparation mechanisms investigation*** will improve understanding and possibly increase signal clearing beyond 99.3%; particularly, study of atomic beam exit-side laser aperturing.
2. A *30 GHz* ***broadband laser*** will allow experimentation on ^{3}He and ^{4}He simultaneously;
3. ***2/16" or greater inner pair gap*** may further improve the far field decay rate. Concerns about axial (z-axis) B-field size summarily reduced this option's importance in this study; and
4. ***1/32" or greater outer to inner pairs spacing*** holds the potential of reduced B_x affording better collimation purity, but at the cost of less confined field.. Initial measurements show improved collimation potential for 1/32" outer to inner pairs spacing.

.

References

1. Kastler, A. Optical Methods of Atomic Orientation and of Magnetic Resonance, J. Opt. Soc. Am., vol. 47, no. 6, pp. 460-464, 1957.
2. Shiner, D.; Dixon, R. Measuring the Fine Structure Constant Using Helium Fine Structure, IEEE Trans. Instrum. Meas., vol. 44, no. 2, pp. 518-521, 1995.
3. Smiciklas, M.; Shiner, D. Determination of the Fine Structure Constant Using Helium Fine Structure, Phys. Rev. Lett., vol. 105, no. 12, pp. 3001-1 to 3001-4, 2010.
4. Rezaeian, N. A Precise Few-Nucleon Size Difference by Isotope Shift Measurements of Helium, Doctorate, University of North Texas, Denton, Texas, 2015.
5. Coey, J. M. D. Rear-Earth Iron Permanent Magnets, Oxford, UK: Clarendon Press, 1996.
6. Arfken, G.; Weber, H.; Harris, F. Mathematical Methods for Physicists, Oxford, UK: Academic Press, 2013.
7. Gauthier, D.; Narum, P.; Boyd, R. Simple, compact, high-performance permanent-magnet Faraday isolator, Opt. Lett., vol. 11, no. 10, pp. 623-625, 1986.
8. COMSOL – Software for Multiphysics Simulation. Available Online: www.comsol.com (Accessed 25 June 2021).
9. Jackson, J. D. Classical Electrodynamics, Berkley, CA: John Wiley & Sons, 1999.
10. Magnetic Field Along The Axis of A Circular Coil Carrying Current. Available Online: vlab.amrita.edu/?sub=1&brch=192&sim=972&cnt=1 (Accessed 2 January 2020).
11. K&J Magnetics | Strong Neodymium Magnets, Rare Earth Magnets. Available Online: www.kjmagnetics.com Accessed 26 June 2021)
12. Feng, G.; Zheng, X.; Sun, Y.; Hu, S. Laser-spectroscopy measurement of the fine-structure splitting 2P1 (triplet) - 2P2 (triplet) of He-4, Phys. Rev. A, vol. 91, no. 3, pp. 030502-1 to -5, 2015.
13. Electromagnetic and Magnetic Software | EM Works. Available Online: www.emworks.com (Accessed 25 June, 2021)
14. Pichanick, F. M. J.; Swift, R. D.; Johnson, C. E.; Hughes, V. W. Experiments on 2^3P State of Helium I. A Measurement of the 2^3P_1-2^3P_2 Fine Structure, Phys. Rev., vol. 169, no. 1, pp. 55 to 78, 1968.
15. Shankar, R. Principles of Quantum Mechanics, New Haven, CT: Plenum Press, 1994.
16. Siegman, A. E. Lasers, Stanford, CA: University Science Books, 1986.